Open Archive Toulouse Archive Ouverte (OATAO)

OATAO is an open access repository that collects the work of Toulouse researchers and makes it freely available over the web where possible

This is an author's version published in: **http://oatao.univ-toulouse.fr/23662**

To cite this version:

Xu, Nan and Monceau, Daniel and Young, David and Furtado, Jader *High temperature corrosion of cast heat resisting steels in CO+CO2 gas mixtures.* (2008) Corrosion Science, 50 (8). 2398-2406. ISSN 0010-938X

High temperature corrosion of cast heat resisting steels in CO + CO$_2$ gas mixtures

Nan Xu [a,1], Daniel Monceau [a,2], David Young [a,*], Jader Furtado [b]

[a] *School of Materials Science and Engineering, University of New South Wales, Sydney NSW 2052, Australia*
[b] *Air Liquide, Centre de Recherche Claude-Delorme, 1 chemin de la Porte des Loges, BP 126-78354 Jouy-en-Josas Cedex, France*

ARTICLE INFO

ABSTRACT

Two commercial variants of the cast heat resistant grade HP40Nb (Fe 25Cr 35Ni, Nb modified) were exposed to CO/CO$_2$ gases at 982 and 1080 °C in order to simulate exposure to the carbon and oxygen potentials realised in steam reformers under normal and overheated conditions. Both alloys developed external chromium rich oxide scales, intradendritic silica precipitates and interdendritic oxide protrusions where primary, interdendritic carbides were oxidised in situ. Surprisingly, the lower silicon content alloy developed a more continuous internal silica layer, thereby slowing external scaling. Intradendritic oxidation was fast in both alloys, and is attributed to interfacial oxygen diffusion. Both alloys underwent rapid internal carburisation, indicating that their oxide scales failed to prevent carbon access to the underlying alloys under these reaction conditions.

1. Introduction

Centrifugally cast tubes of heat resisting alloys are widely used in reformers and other high temperature chemical process units. In reformers, the tubes function as heat exchangers, being exposed on their outside to combustion gases and on their inside to process gases. The gases are those in the process

$$CH_4 + H_2O \quad CO + 3H_2$$

and are both carburising and mildly oxidising. Operating temperatures are a little below 1000 °C, but excursions up to almost 1100 °C can occur.

The alloys chosen for this service are chromium bearing austenitic steels or nickel base alloys, of dendritic microstructure with chromium rich carbides occupying interdendritic regions and forming much smaller secondary precipitates. These alloys survive the process environment by forming a protective chromium rich oxide scale. In purely oxidising conditions [1 3], the alloys form duplex scales of chromia overlaid by manganese rich spinel. A silicon rich sublayer can also develop at the scale alloy interface [1 5]. The limited information available [6,7] for the simultaneous attack on these alloys by both carbon and oxygen indicates that similar reaction products are formed.

An alloy grade frequently chosen for service in reformers is HP40Nb. Its compositional specification is seen in Table 1 to be quite wide, particularly with respect to minority alloy constituents. It is known [8,9] that changing the concentration of manganese and silicon in wrought alloys can alter their oxidation rates considerably. Commercial alloys conforming to the HP40Nb specification can differ significantly in composition, and the aim of the present work was to determine whether these variations would affect corrosion resistance under simulated service conditions.

2. Experimental

Two as cast alloy tubes were obtained from different commercial suppliers. The materials will be referred to here as A1 and A2. Their compositions were measured using energy dispersive analysis of X rays (EDAX) in a field emission scanning electron microscope (FESEM). In addition, alloy aluminium and titanium levels were measured by glow discharge mass spectrometry (GDMS), and both carbon and sulphur concentrations were determined by combustion analysis using a LECO CS 444. All results are shown in Table 1. Both alloys were austenitic and had typical cast micro structures, as seen in Fig. 1. Here the carbides have been revealed by stain etching with Murakami's reagent. Identification of the large interdendritic carbides was confirmed by EDAX. In addition, very fine secondary carbides were present within the austenitic dendrites.

Rectangular coupons (10 × 5 × 2 mm) were machined from the tube walls, with their major surfaces parallel to the tube radius. These were prepared for reaction by grinding to a 600 grit finish and ultrasonically cleaning in acetone.

The alloys were exposed to a flowing gas mixture of CO 4.3% CO$_2$, at temperatures of 982 and 1080 °C and a total pressure of approximately 1 atm. These conditions were used to simulate the

* Corresponding author. Tel.: +61 2 9385 4322; fax: +61 2 9385 5956.
E-mail addresses: Nxu@hrl.com.au (N. Xu), Daniel.Monceau@ensiacet.fr (D. Monceau), D.Young@unsw.edu.au (D. Young).
[1] Present address: HRL Technology Pty Ltd, Mulgrave Vic 3170, Australia.
[2] On sabbatical leave from CIRIMAT CNRS INPT UPS ENSIACET, 31077 Toulouse, France.

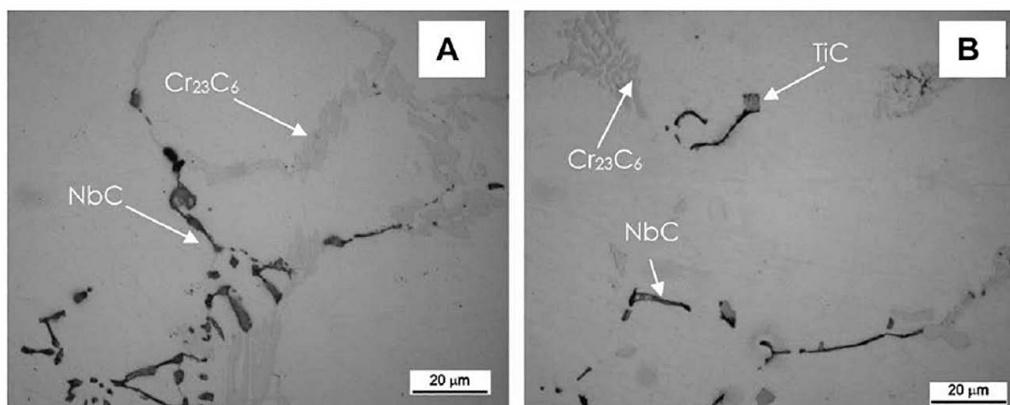|	Ni	Cr	Nb	Si	Al	Ta	Mo	Mn	W	Ti	C	S
HP40Nb	33–37	24–28		2.5 max			0.5 max	2.0 max			0.35–0.75	0.04 max
A1	32.6	25.5	1.0	1.5	8.2[a]	0.2	0.1	1.3	0.4	340[a]	.39	.010
A2	34.9	26.0	1.4	0.6	560[a]	0.2	0.1	0.7	1.0	.14	.41	.006

[a] ppm.

Fig. 1. Microstructures of as-received cast alloys.

Table 2
Calculated carbon and oxygen activities for $CO + CO_2$ gas mixture

Gas mixture	$T/°C$	p/atm	a_C	p_{O_2}/atm
95.7% CO + 4.3% CO_2	982	1	0.20	7×10^{-18}
95.7% CO + 4.3% CO_2	1080	1	0.06	3×10^{-16}

carbon and oxygen potentials realised in steam reformers under normal and overheated conditions. The total pressure in the laboratory experiments was much lower than in a reformer (typically 10–40 atm), and the gas mixture was adjusted to yield the desired potentials. Corresponding values of the carbon activity, a_C, and oxygen potential calculated from the equilibria

$$2CO \rightleftharpoons CO_2 + C \qquad (1)$$

$$CO_2 \rightleftharpoons CO + 1/2 O_2 \qquad (2)$$

are shown in Table 2.

Reaction products were analysed on the sample surfaces by X-ray diffraction (XRD) using Cu Kα radiation. Reaction morphologies and phase constitutions were investigated using conventional metallographic techniques, including transmission electron microscopy (TEM).

3. Results

Both alloys suffered partial scale spallation during cooling after reaction, the affect being more severe in the case of A2. Obviously, weight change data could not be used to assess the extent of reaction. Analysis of the surfaces by XRD showed that MCr_2O_4 spinel and Cr_2O_3 were the external corrosion products on all samples. Cross-sectional images of the surface regions of reacted samples are shown in Figs. 2 and 3, where a two-layered external scale is apparent. Analysis by EDAX showed that the dark outer layer was $MnCr_2O_4$ and the inner layer Cr_2O_3. Scale thicknesses, X, were measured metallographically, taking the maximum values observed to represent unspalled regions. As seen in Fig. 4, scale thicknesses increased with time at 982 °C according to approximately parabolic kinetics,

$$X^2 = 2k_p t \qquad (3)$$

where t is time and k_p the parabolic rate constant. Alloy A1 scaled significantly faster than A2 at this temperature. At 1080 °C, however, the scaling kinetics were subparabolic (Fig. 4), and rates were similar for the two alloys. Both the spinel and chromia sublayers thickened with time, the spinel constituting a greater fraction of the scale on alloy A1.

Growth of the chromium-rich external scale was accompanied by depletion of chromium and the disappearance of secondary carbides within subsurface regions of the alloys. As seen in Figs. 2 and 3, the depth of carbide dissolution increased with time. The kinetics of this process (not shown) were approximately parabolic at 982 °C, but subparabolic at 1080 °C.

The internal oxidation zone immediately beneath the alloy surface is seen in Figs. 2 and 3 to contain both large interdendritic oxides and, at more shallow depths, smaller precipitates within the austenite. The latter developed into an almost continuous internal layer with increased time and temperature. This morphological evolution was much more pronounced in A2 than in A1. Analysis of the internal oxides by EDAX showed that the interdendritic material was a mixture of chromium oxide (grey) and silicon-rich oxide (black) (Fig. 5), and occasionally almost pure SiO_2 (Fig. 6). The intradendritic precipitates immediately beneath the scale were found to have a composition close to that of SiO_2 (Fig. 6). This phase was identified by selected area diffraction measurement in the TEM (Fig. 7) as cristobalite. The light grey, almost white precipitates visible in the SEM images are NbC. The internal oxidation zone was, in fact, more complex, involving also minority amounts of oxides containing aluminium, titanium and niobium, as identified by TEM. A more detailed account of these will be published elsewhere.

Estimates of internal oxidation kinetics were attempted by measuring the average depths of intradendritic precipitation, X_i. No measurement was possible for samples reacted at 982 °C for 100 h. Data for 1080 °C is shown in Fig. 8, where the kinetics are seen to be approximately parabolic, and considerably faster for alloy A1. Rates of interdendritic oxidation were assessed by
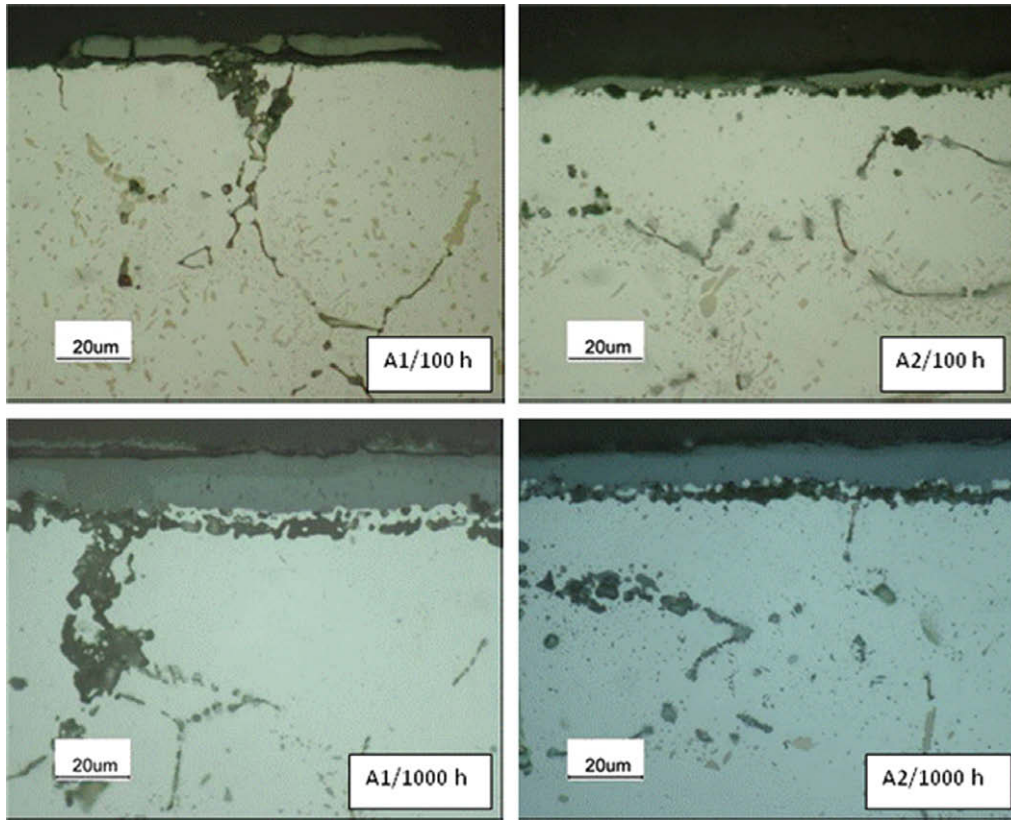
Fig. 2. Cross-sections of alloy surfaces after reaction at 982 °C for indicated times.
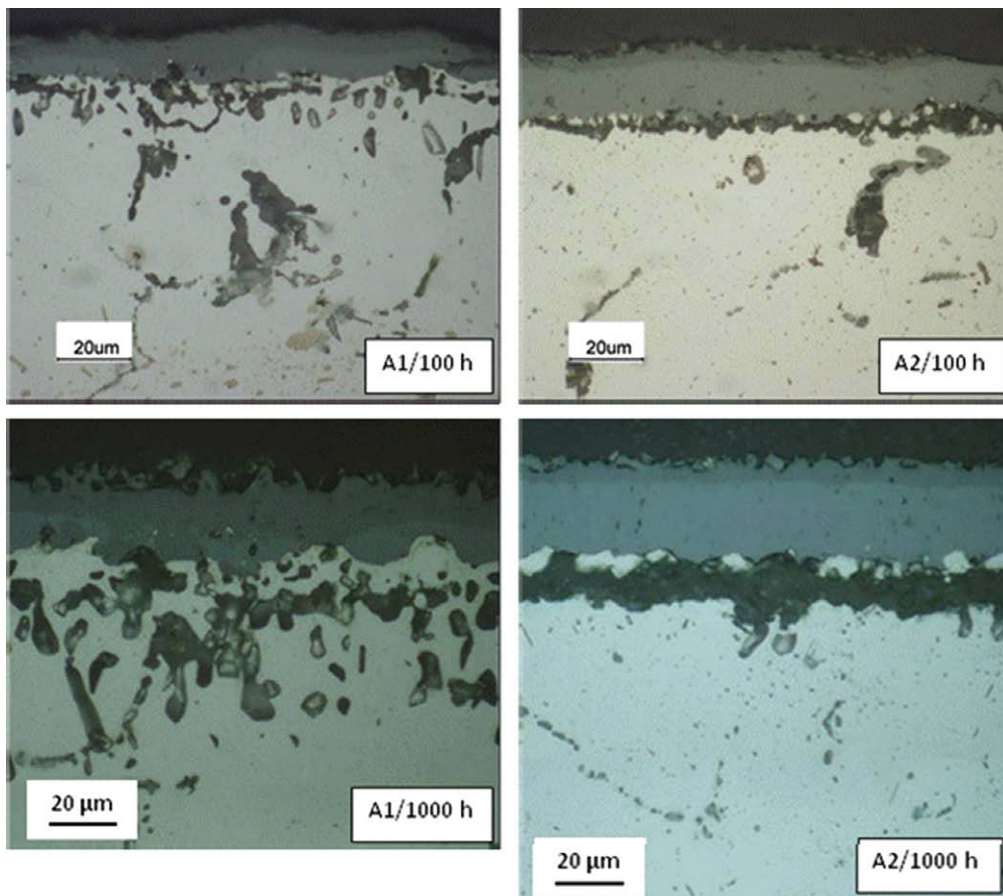

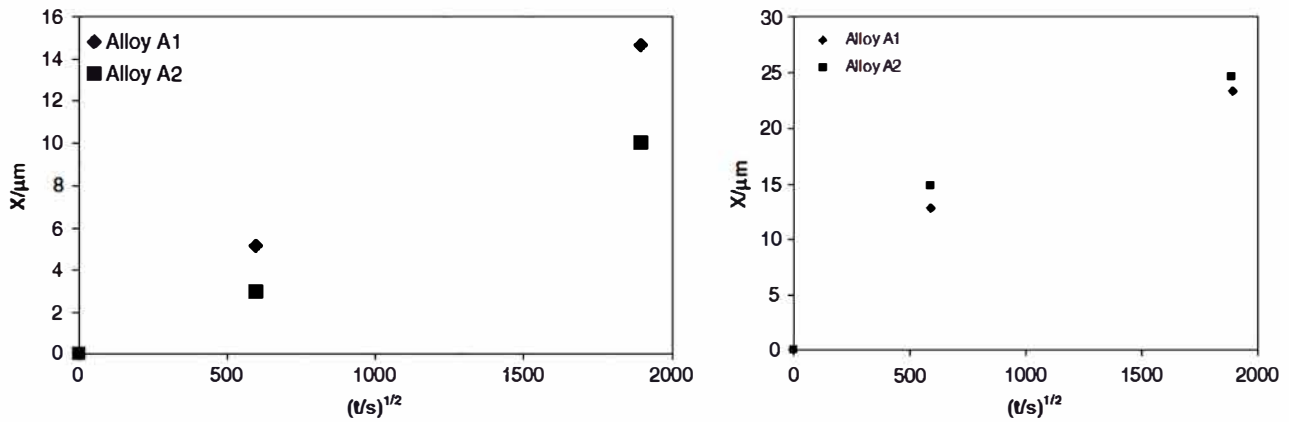**Fig. 3.** Cross-sections of alloy surfaces after reaction at 1080 °C for indicated times.

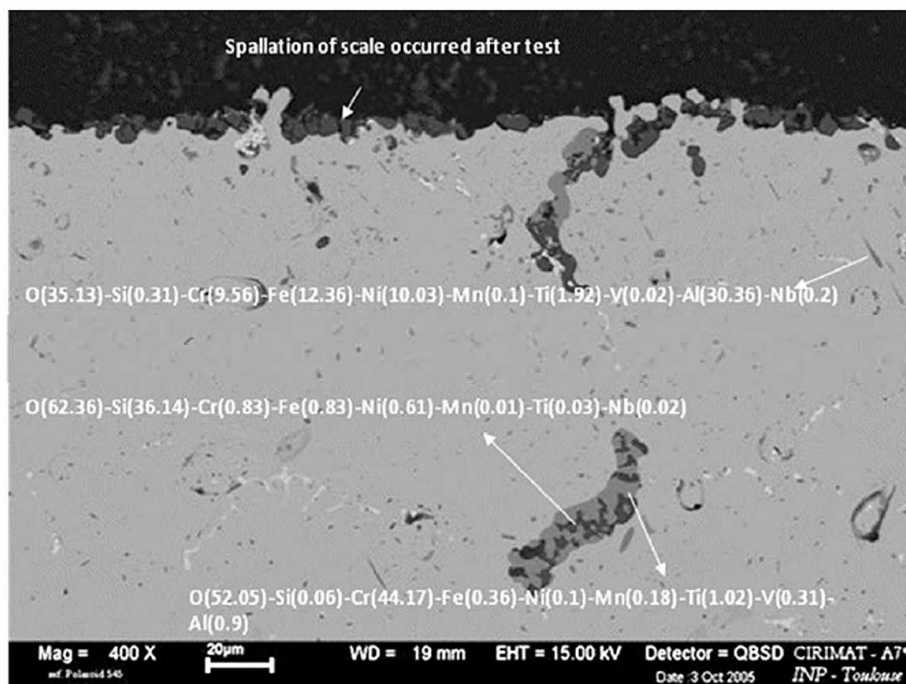Fig. 4. Scalegrowth kinetics at 982 °C (left) and 1080 °C (right).

Fig. 5. EDAXanalysis of internal oxides formed in A1 after 1000 h at 1080 °C.

measuring the maximum depth of oxide penetration. The kinetics at 982 °C were roughly parabolic, but at 1080 °C were subparabolic (Fig. 9).

In addition to internal oxidation, subsurface carbide dissolution and internal carburisation were evident. Deep within the alloy, the original interdendritic carbides were still present, but additional fine precipitates had developed within the austenite dendrites. These precipitates had the metallographic appearance of carbide, but were too fine for microanalysis. Bulk chemical analysis was used to confirm that internal carburisation had occurred. The aver age carbon concentration in reacted alloy A1 was determined by analysing the entire sample after carefully removing the external scale. The results reflected averages of the carburised interiors and the carbide free subsurface regions. Correction for this effect led to the estimates shown in Table 3 for carbon levels in the alloy interior. The carbon content in alloy A1 is seen to have increased with reaction at both temperatures. The relatively small carbon uptake was confirmed using quantitative image analysis to esti mate the carbide volume fraction, f_v, in reacted alloys. As seen in

Table 3, the measured value of f_v increased with reaction for alloy A1. Similar measurements for alloy A2 showed that f_v increased from an initial value of 8.4% to 9.0 and 11.1% after 1000 h reaction at 982 and 1080 °C, respectively. Carburisation kinetics could not be measured, as the entire sample width appeared in all cases to contain a uniform volume fraction of carbide.

4. Discussion

Reaction morphologies developed by the two alloys were very similar. In most respects, the reaction products were the same as those produced by oxidation in non carburising environments [3,10]: an external chromium rich oxide scale, a chromium de pleted alloy subsurface region, interdendritic carbide oxidation and a shallow zone of internally precipitated oxides within the austenite dendrites. In addition, increased numbers of fine, second ary carbides formed in the interior of both alloys. Oxidation and carburisation processes are discussed separately.
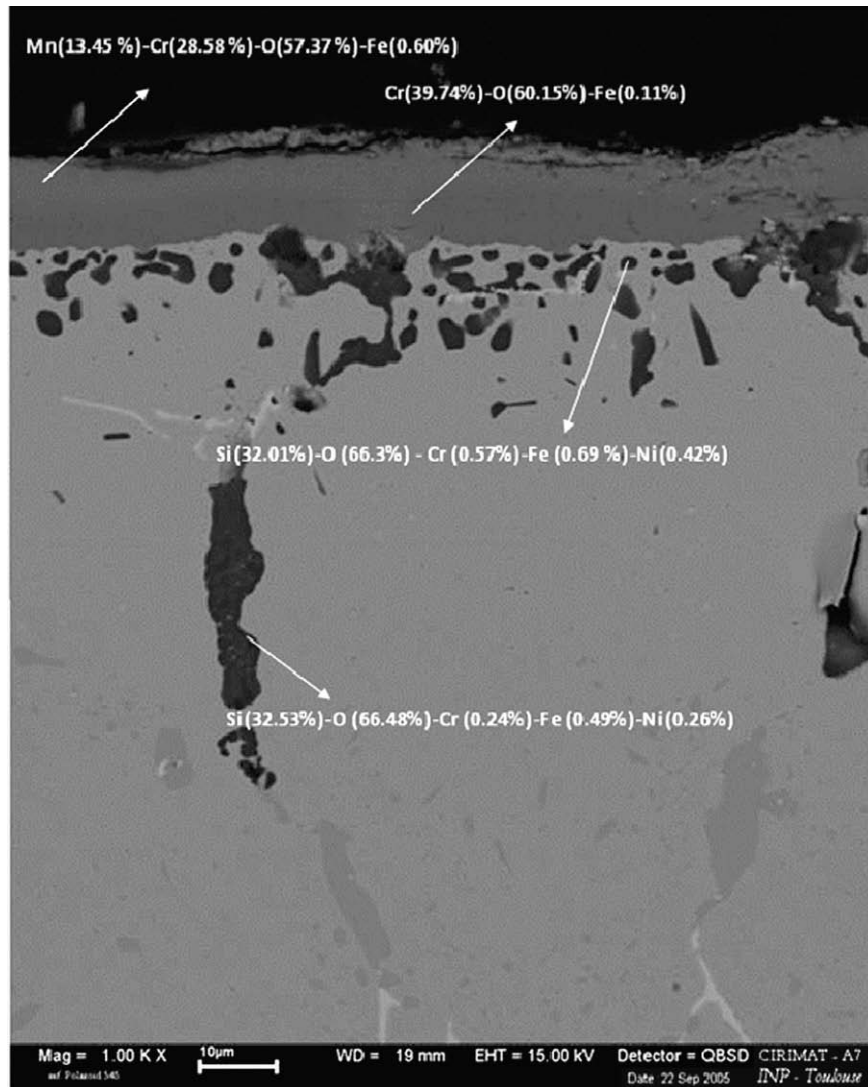
Fig. 6. EDAX analysis of internal oxides in A1 after 100 h at 1080 °C.

4.1. Oxidation

The observed pattern of oxide reaction products is consistent with local equilibrium within the reaction zone: the oxides Cr_2O_3, $MnCr_2O_4$, SiO_2 and Al_2O_3 are all stable under the reaction conditions, but the oxygen potentials were too low to form NiO. Furthermore, the sequence of oxides reflected the existence of a gradient in oxygen activity. Thus the least stable spinel was in contact with the gas, above the more stable chromia. The even more stable silica and alumina were precipitated at the lower oxygen activities prevailing within the alloy. At variance with this description was the observation of interdendritic chromium oxide at much greater depths than the intradendritic silica. This reflects the very different oxygen potential profile supported by rapid boundary diffusion.

External scaling kinetics were approximately parabolic, indicating diffusion control. Values of k_p found from the application of Eq. (1) were used to calculate equivalent weight uptake rate constants, k_w, using the densities of Cr_2O_3 and $MnCr_2O_4$, weight fractions of oxygen in these compounds and measured sublayer thicknesses. Data obtained at 1080 °C was approximated as parabolic for this purpose. Comparison in Fig. 10 with weight uptake rates for a variety of chromia forming alloys [11] shows that both alloys grew scales at rates to be expected of superior chromia formers. Interest

ingly, alloy A2 scales significantly slower than does A1 at 982 °C, but no significant difference in rate is apparent at 1080 °C.

The reasons for the superior scaling resistance of these steels are of interest, as well as practical importance. In the same way, reasons for the difference between rates for the steels at 982 °C and their similarity at 1080 °C attract attention. It has long been known [1 3] that heat resisting steels, which invariably contain small but significant amounts of silicon, develop a thin, silicon rich oxide layer beneath their chromia scales. This layer is thought to be important in slowing the rate of chromia scale growth by acting as a partial barrier to diffusion. On this basis, the higher silicon content of alloy A1 would be expected to pro vide a more rapidly formed silica layer, leading to slower scaling kinetics. This benefit was clearly not available at 982 °C, as seen in Fig. 4.

Under the reaction conditions studied in the present work, silica forms as internal precipitates rather than a surface layer. As seen in Fig. 2, alloy A2 forms internal silica more quickly than alloy A1, and develops a more continuous internal layer of silica at 982 °C. The more effective barrier to outward chromium diffusion provided by this layer would account for the slower growth of external chromia scale on alloy A2. At 1080 °C, the same pattern of internal silica layer development is evident (Fig. 3), but the scale thickness mea surements in Fig. 4 show no apparent benefit to alloy A2.
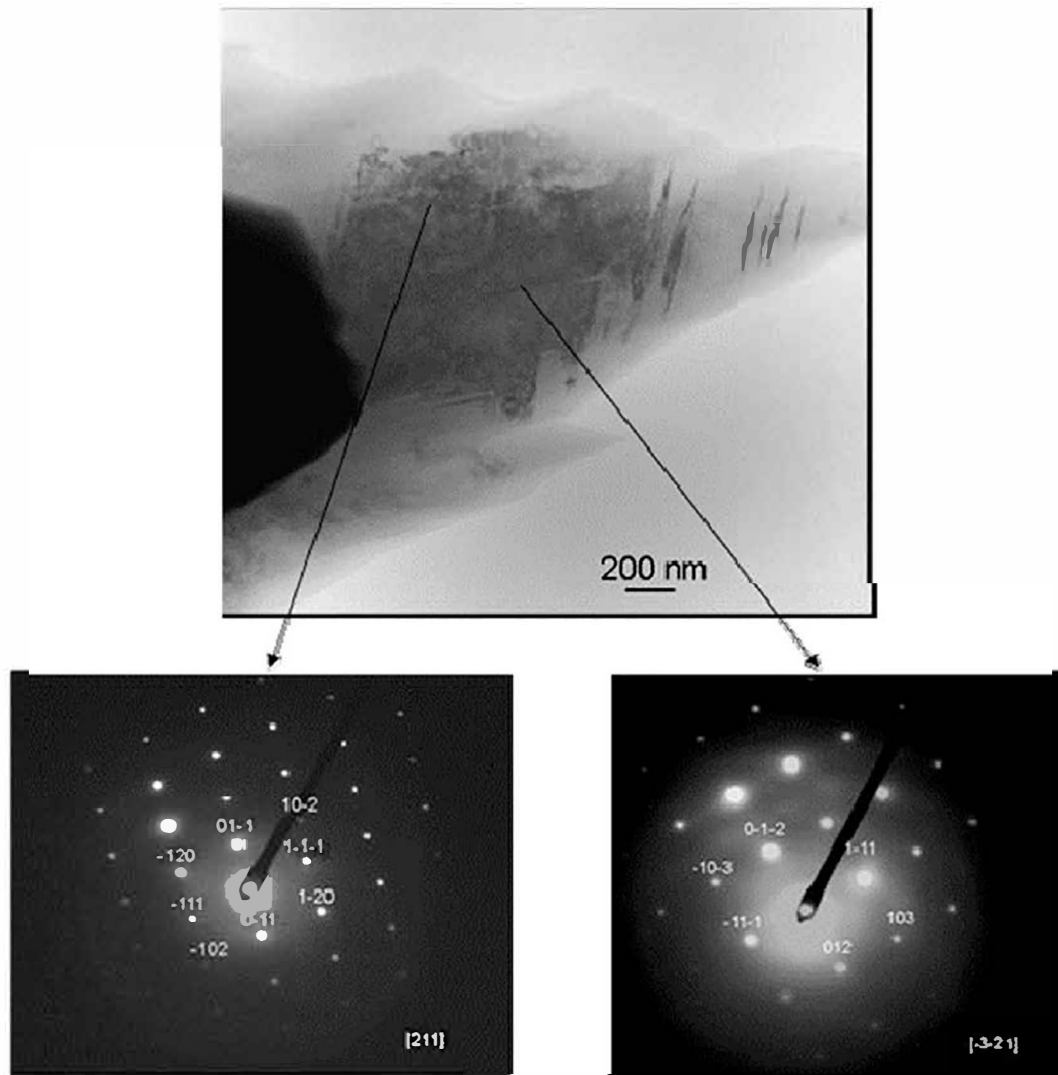
Fig. 7. TEM bright field image and SAD patterns: silica precipitate in A1 identified as tetragonal cristobalite.
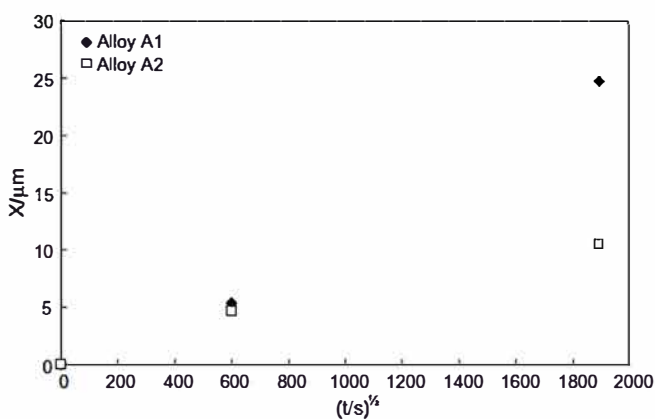

Fig. 8. Intradendritic oxidation depths at 1080 °C.

Examination of the scale cross sections in Fig. 3 reveals that the relative thicknesses of the chromia and spinel layers differ between the two alloys. The formation of an outer spinel layer is common for such alloys. It results from the rapid diffusion of manganese through Cr_2O_3 [12], and the stability of $MnCr_2O_4$. The differ

ent amounts of spinel formed on the two alloys reflect their relative manganese levels, and the greater amounts formed at the higher temperature result from the faster diffusion of manganese through the underlying chromia. Growth of the spinel layer is of some benefit in reducing overall scaling rate. As shown by Douglass and Armijo [8], spinel layer growth is much slower than chromia growth. Thus alloy A1, with its higher manganese content, reacts to form scale in which a substantial fraction of the chromium is present in slow growing $MnCr_2O_4$ rather than Cr_2O_3. At 1080 °C, this benefit offsets the failure of this alloy to develop a continuous silica layer. At 982 °C, however, much less spinel forms, and this benefit is not available.

Alloy subsurface reaction zones were also very similar. Growth of chromium rich oxide scales caused depletion of chromium in the alloy. The lowered chromium concentration led to secondary carbide dissolution

$$Cr_{23}C_6 \quad 23\underline{Cr} + 6\underline{C} \tag{4}$$

and might have caused partial dissolution of the primary, interdendritic carbides. However, large amounts of primary carbide were oxidised in situ
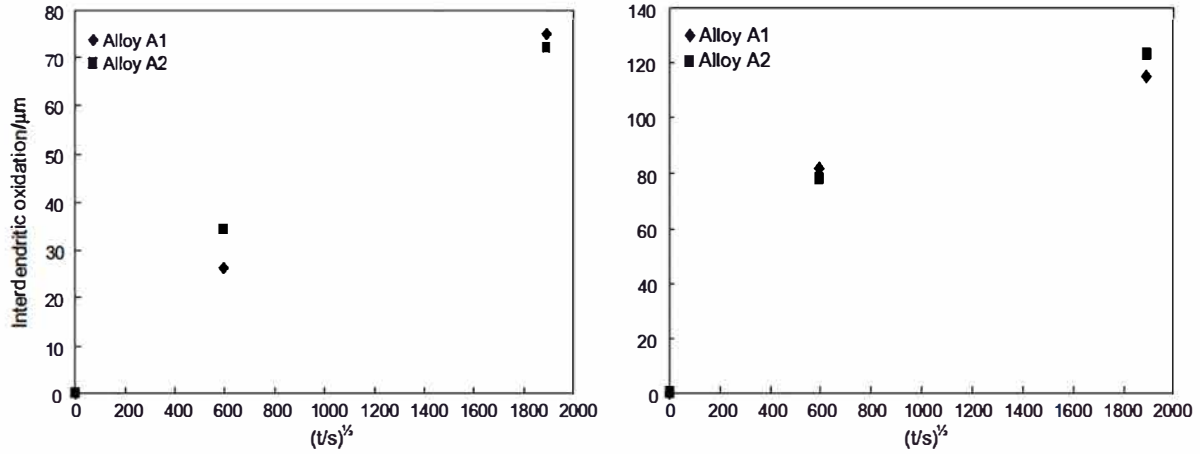
$$2Cr_{23}C_6 + 69O \quad 23Cr_2O_3 + 12C \tag{5}$$

Fig. 9. Interdendritic oxidation: at 982 °C (left) and 1080 °C (right).

Table 3
Carbon uptake by alloy A1 during carburisation

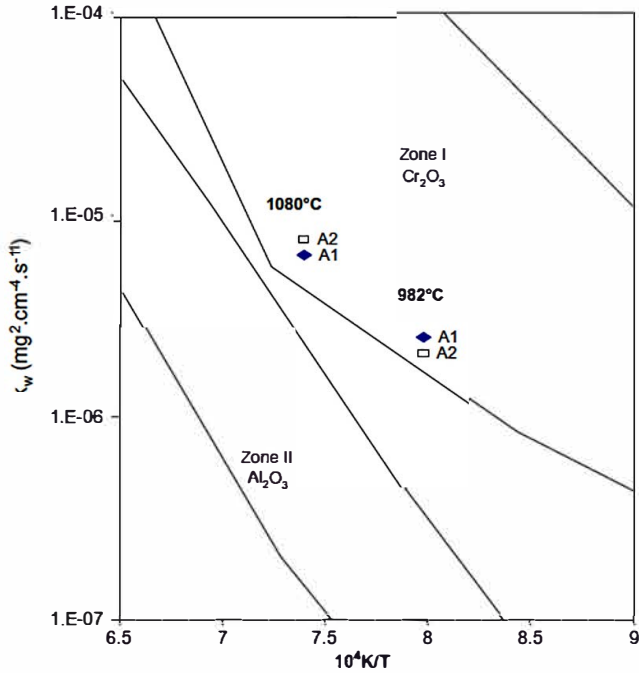| Sample	C (wt%)	S (wt%)	f_v ($Cr_{23}C_6$)/%	
			Calculated	Measured
Before reaction	0.39	0.010	7.9	8.3
1000 h at 982 °C	0.50	0.012	10.1	9.1
1000 h at 1080 °C	0.57	0.010	11.5	10.2

Fig. 10. Comparison of measured scaling rates with literature data collected by Hindam and Whittle [11].

as has been observed before in the oxidation of cast heat resisting steels [10,13].

As already noted, the depth of interdendritic oxidation was much greater than that of intradendritic silica precipitation. Both reactions followed approximately parabolic kinetics

$$X_i = 2k_p^{(i)}t \qquad (6)$$

where X_i is the internal oxidation depth reached in time, t, and $k_p^{(i)}$ is the parabolic rate constant. If the internal oxidation processes are sustained by volume diffusion of dissolved oxygen through the alloy matrix, then the rate is given by Wagner's theory [14,15] as

$$k_p^{(i)} = \frac{D_o N_o^{(s)}}{\nu N_M} \qquad (7)$$

or

$$k_p^{(i)} = \frac{\pi}{D_M}\left(\frac{D_o N_o^{(s)}}{\nu N_M}\right)^2 \qquad (8)$$

Here $N_o^{(s)}$ is the dissolved oxygen concentration (mole fraction) at the alloy surface, D_o is the volume diffusion coefficient for oxygen and D_M that for the reacting solute metal, M, ν is the stoichiometric coefficient for the precipitated oxide MO_ν and N_M is the bulk concentration of M. Oxygen diffusion alone is rate controlling if $D_M N_M \ll D_o N_o^{(s)}$, and in this limiting case Eq. (7) holds. If both species diffuse into the precipitation zone, $N_o^{(s)}/N_M \ll D_M/D_o \ll 1$ and Eq. (8) represents this mixed control. In both cases, the rate of penetration is inversely proportional to N_M. Values of $k_p^{(i)}$ for the interdendritic process at 982 °C were about 1.5×10^{-11} cm^2 s^{-1} for both alloys. This value is very close to measurements made at 1000 °C on a variety of cast heat resisting alloys [3,10,13]. If $N_o^{(s)}$ is controlled by equilibrium with the chromia scale, then it is calculated [10] from Eq. (7) that for internal chromium oxidation $k_p^{(i)} = 6 \times 10^{-18}$ cm^2 s^{-1}, and from (8) that it is 10^{-24} cm^2 s^{-1}. It is clear that inward oxygen transport is very much faster than would be predicted for alloy matrix diffusion. It is therefore concluded, in agreement with earlier work, that the rapid rate of interdendritic oxidation is supported by fast oxygen diffusion along the oxide austenite interfaces, which provide almost continuous pathways between the alloy surface and its interior. This also explains why the rates for these two alloys and others of rather different N_{Cr} level are nonetheless equal: the interfacial diffusion process is largely independent of alloy chemistry.

The intradendritic precipitation of silica might be expected to be controlled by alloy matrix diffusion, at least in the case of alloy A1 where a dispersed precipitate is formed. At 1080 °C, values of $k_p^{(i)}$ were estimated from Fig. 8 as 2×10^{-12} and 3×10^{-13} cm^2 s^{-1} for A1 and A2, respectively, and these are now compared with the values predicted from Eqs. (7) and (8). The necessary data are not available for austenite of the compositions used here. However, values appropriate to a nickel matrix have been reported by Park and Altstetter [16] for D_o and $N_o^{(s)}$, and by Swalin et al. [17] for D_{Si}. According to Sievert's equation

$$N_o^{(s)} = K p_{O_2}^{1/2} \qquad (9)$$

the value of $N_O^{(s)}$ varies with p_{O_2}, which therefore must be specified. The value of p_{O_2} at the scale alloy interface is controlled in the present case by the equilibrium

$$Cr_2O_3 \quad 2Cr + 1.5O_2 \tag{10}$$

and can be calculated from a knowledge of the activity a_{Cr}. If a_{Cr} in the depleted surface is estimated as 0.15, then a value of p_{O_2} 10^{19} atm is calculated if unit activity is assumed for Cr_2O_3. The value $N_O^{(s)}$ 1.1×10^{8} results. Taking $D_O = 2.3 \times 10^{8}$ cm^2 s^{1} and $D_{Si} = 1.6 \times 10^{10}$ cm^2 s^{1} together with $N_{Si} = 2.9 \times 10^{2}$ and 1.2×10^{2} in A1 and A2, respectively, it is found that the conditions for Eq. (8) are met. On this basis it is expected that internal oxidation of silicon will be supported by diffusion of both reactants. The obvious enrichment of silicon in the precipitation zone confirms the validity of this description. However, the values of $k_p^{(i)}$ calculated from (8) are 3×10^{19} and 2×10^{18} cm^2 s^{1} for A1 and A2. If instead the highest possible value for the interfacial oxygen activity, that of the ambient atmosphere, is specified, then values for $k_p^{(i)}$ of 6×10^{16} and 4×10^{15} cm^2 s^{1} are calculated for the two alloys.

Clearly, inward oxygen diffusion is much faster than predicted from the data for D_{Si}, D_O and $N_O^{(s)}$ in pure nickel. Given the strong interactions between dissolved oxygen and the gradients in metal solutes [18], it is not surprising that the inward oxygen flux, J_O, is accelerated according to the multicomponent diffusion description:

$$J_O \quad D_{OAl}\nabla C_{Al} \quad D_{OSi}\nabla C_{Si} \quad D_{OO}\nabla C_O \tag{11}$$

Here the D_{ij} are the diffusion coefficients relating the flux in component i to the gradient in concentration, C_j. The thermodynamic interactions between oxygen and both chromium and silicon are strongly negative, and negative D_{Oj} coefficients result. The gradients in chromium and silicon are both positive, and steeper than that in oxygen, leading to large increases in the oxygen flux.

The preceding analysis does not explain the relative rates of internal silicon oxidation in the two alloys. According to the classical diffusion theory of internal oxidation, as expressed in Eqs. (8) and (9), the rate of penetration is decreased as N_{Si} increases. However, alloy A1 with its higher silicon content, oxidises to greater depths than does the low silicon alloy A2. A related problem is the different degree of silicon enrichment evident in the internal oxidation zones of the two alloys.

The enrichment factor, α, is defined as the mole fraction ratio

$$\alpha \quad \frac{N_{SiO_2}}{N_{Si}} \tag{12}$$

It is predicted from the Wagner theory to be

$$\alpha \quad \{h\sqrt{\pi}\exp(h^2)\mathrm{erfc}(h)\}^{1} \tag{13}$$

where

$$h \quad \gamma\sqrt{\frac{D_O}{D_{Si}}} \quad \gamma \quad \sqrt{\frac{k_p^{(t)}}{4D_O}} \tag{14}$$

Using experimentally observed values for $k_p^{(i)}$ and the coefficients quoted above for diffusion in nickel, the predictions for α shown in Table 4 were arrived at. Measured enrichment factors are seen to be in reasonable agreement. They are, moreover, consistent with the different oxidation rates. Thus the slower oxygen penetration rate in A2 allows more silicon diffusion towards the surface, where it forms an enriched and eventually continuous oxide zone. Unfortunately, the relative rates cannot be predicted from elementary diffusion theory. Clearly, the rate of silicon diffusion is not determined simply by the gradient in silicon concentration and a binary diffusion coefficient, as is assumed in deriving Eq. (8). Instead, the silicon flux needs to be evaluated from a multicomponent diffusion expression

Table 4
Silicon enrichment (α) in internal precipitation zones at 1080 °C after 1000 h reaction

Alloy	Measured	Calculated
A1	6	10
A2	18	22

$$J_{Si} \quad \sum_{j=1}^{n-1} D_{Si,j}\nabla C_j \tag{15}$$

for a system of n components.

The superior ability of alloy A2 to resist internal attack and develop a silica sublayer which affords some degree of protection is an advantage. An understanding of this phenomenon cannot be developed without a knowledge of the relevant thermodynamic interactions between alloy solutes, or an empirical evaluation of the $D_{Si,j}$ in (15). Since, furthermore, alloys of this sort frequently contain minority amounts of reactive elements, the contents of which are unknown in the present cases, no further discussion is attempted.

4.2. Carburisation

Both alloys underwent internal carburisation, developing metallographically visible chromium rich carbide precipitates. In the case of alloy A1, chemical analysis (Table 3) confirmed that the precipitates represented carbon uptake by the alloy, and not merely an ageing process. Rates of internal carburisation are controlled by inward carbon diffusion, and can be calculated from Eq. (7), (8), using D_C and $N_C^{(s)}$, the diffusion coefficient and solubility of carbon in the metal matrix.

If all chromium is precipitated from the alloy, the remaining metal matrix can be approximated as an Fe Ni alloy. Values of D_C [19] and $N_C^{(s)}$ [20] are available for binary Fe Ni alloys at 1000 °C, close to the experimental temperature of 982 °C. Carbon solubility is, of course, dependent also on the carbon activity at the alloy scale interface. The value of this activity depends on the rate at which carbon is transferred through the oxide scale. Ideally, the scale is impermeable to carbon, and the alloy is protected against carburisation. Although Cr_2O_3 has negligible solubility for carbon [21], Grabke et al. [22] have shown that chromia scales do transmit carbon. Furthermore, it appears from experiments conducted in mixed gases [23] that the carbon permeability of chromia scales depends on gas composition. That work showed that chromia scales grown in $N_2/CO/CO_2$ mixtures were permeable to carbon. Accordingly, the present observation that scales produced in CO/CO_2 transmit carbon to the underlying alloy is to be expected.

A maximum carburisation rate can be calculated on the basis that the carbon activity at the alloy surface is the same as in the gas, $a_C = 0.2$. In this case, $N_C^{(s)}$ 3.7×10^{3} and $D_C = 3.2 \times 10^{7}$ cm^2 s^{1}. Taking $D_{Cr} = 7.2 \times 10^{12}$ cm^2 s^{1} [24] and $N_{Cr} = 0.29$, it is found that the conditions for Eq. (7) are met. Calculation from (7) using $\nu = 0.345$ (an average of the values for Cr_7C_3 and $Cr_{23}C_6$) yields $k_p^{(i)}$ 1.2×10^{8} cm^2 s^{1} for both alloys. This corresponds to a depth of more than 900 µm after 100 h, and essentially complete carburisation of the 2 mm thick samples, in agreement with observation. It is therefore concluded that the chromium rich oxide scales grown on these alloys do not provide effective barriers to carbon ingress from CO/CO_2 gas. It should be noted, however, that the presence of H_2O in the gas is likely to reduce the carbon permeability of chromia scales. On this basis, better performance could be expected in reformer environments.

5. Conclusions

Two commercial variants of the standard HP40Nb grade were found to exhibit significantly different oxidation behaviour in CO/CO_2 gases. Both alloys are superior chromia formers, but the one with lower manganese and silicon levels scaled more slowly at 982 °C. Despite its lower silicon level, this alloy formed internal silica more quickly, and developed a more continuous layer, thereby slowing chromium diffusion and scale growth.

Both alloys oxidised internally, producing interdendritic oxides to great depth, and more shallow zones of intradendritic silica. The interdendritic oxidation process was supported by boundary diffusion of oxygen at the same rate in these two, and other, heat resisting alloys. Intradendritic internal oxidation was a slower process, but nonetheless much faster than would be predicted from binary diffusion data for oxygen in nickel. This effect, and the superior performance of the low silicon alloy are suggested to be the results of thermodynamic interactions between interstitial oxygen and substitutional alloy solutes.

Both alloys carburised rapidly, indicating that their oxide scales failed to exclude carbon when exposed to CO/CO_2 gases.

Acknowledgements

References

[1] K. Ledgeff, A. Rahmel, M. Schorr, Werkst. Koprros. 30 (1979) 767.
[2] M.J. Bennett, J.B. Price, J. Mater. Sci. 16 (1981) 170.
[3] D.J. Young, High Temp. Technol. 1 (1982) 101.
[4] H.E. Evans, D.A. Hilton, R.A. Holm, S.J. Webster, Oxid. Met. 19 (1983) 1.
[5] A.G. Revsz, F.P. Fehlner, Oxid. Met. 15 (1981) 297.
[6] P. Tomas, D.J. Young, D.L. Trimm, in: Proc. Int. Congress Met. Corros., National Research Council of Canada, Ottawa 1984, 1, 58.
[7] D.R.G. Mitchell, D.J. Young, W. Kleeman, Corrosion 92, NACE, Houston, TX 1992, Paper 302.
[8] D.L. Douglass, J.S. Armijo, Oxid. Met. 2 (1970) 207.
[9] B. Li, B. Gleeson, Oxid. Met. 65 (2006) 101.
[10] N. Belen, P. Tomaszewicz, D.J. Young, Oxid. Met. 22 (1984) 227–245.
[11] H. Hindam, D.P. Whittle, Oxid. Met. 18 (1982) 245.
[12] R.E. Lobnig, H.P. Schmidt, K. Hennesen, H.J. Grabke, 37, 1992, 81.
[13] P. Becker, D.J. Young, Oxid. Met. 67 (2007) 267–277.
[14] C. Wagner, Z. Elektrochem. 63 (1959).
[15] R.A. Rapp, Corrosion 21 (1965) 382.
[16] J.-W. Park, C.J. Altstetter, Metal. Trans. A 18A (1987) 43.
[17] R.A. Swalin, A. Martin, R. Olson, Trans. AIME 209 (1957) 936.
[18] D.P. Whittle, D.J. Young, W.W. Smeltzer, J. Electrochem. Soc. 123 (1976) 1073–1079.
[19] S.K. Bose, H.J. Grabke, Z. Metallkd. 69 (1978) 8.
[20] T. Wada, H. Wada, J.F. Elliott, J. Chipman, Metal. Trans. 2 (1971) 2199.
[21] I. Wolf, H.J. Grabke, Solid State Commun. 54 (1985) 5.
[22] H.J. Grabke, K. Ohla, J. Peters, I. Wolf, Werkst. Korros. 34 (1983) 495.
[23] X.G. Zheng, D.J. Young, Oxid. Met. 42 (1994) 163.
[24] K. Monura, H. Suto, H. Oikaua, Nippon Kink. Gakk 28 (1964) 188.